Dynamic Article Links ▶

PAPER

Change in the magnetostructural properties of rare earth doped cobalt ferrites relative to the magnetic anisotropy

S. R. Naik and A. V. Salker*

The superparamagnetic properties of the doped cobalt ferrite nanocrystals have been demonstrated. The significance of the sol–gel autocombustion method in yielding the as obtained doped cobalt ferrite oxide powder in the nano-range has been very well complemented with structural, dimensional and morphological analytical techniques such as X-Ray Diffraction (XRD), Transmission Electron Microscopy (TEM), particle size analysis and Scanning Electron Microscopy (SEM). The lattice strain and lattice parameters have been calculated by making use of the Williamson–Hall extrapolation. The valence states of the metal ions and single phase formation of the polycrystalline oxides have been confirmed with the help of X-ray Photoelectron Spectroscopy (XPS) and Raman Spectroscopy. The magnetic measurements M–H and M–T have been carried out demonstrating a change in the magnetic moment and a superparamagnetic–ferrimagnetic transition in the ferrite system. The influence of the distribution of the metal ions in the crystal lattice and the dimensions of the ferrite oxides on the resultant magnetic properties has been demonstrated. The contribution of the spin–orbit coupling generating from the Co^{2+} ions in the octahedral lattice towards higher magnetic anisotropy and hence the magnetic properties is investigated. The results provide an insight into the inter-relationship of the particle dimension, the spin–orbit coupling and the resulting superparamagnetic property.

Introduction

Magnetic spinel ferrites have captured the global market and grabbed the attention of many researchers due to their fascinating and exotic electromagnetic properties. The ease of preparation and the stability of these materials under various conditions have added a lot of significance for their use in the technological industry. The variation that is brought about in the physico-chemical and the electromagnetic properties due to a change in the particle dimension has encouraged many researchers around the globe to synthesize these materials with novel properties. The magnetic,[1–3] electrical[4,5] and magneto-optical[6,7] properties of the pristine and doped cobalt ferrites have prioritized them to be the most widely used ferrite systems in the manufacturing of magnetic recording devices and magnetic fluids.[8,9] Magnetic nanocrystals have been of great interest over the past several years for the fundamental understanding of nanomagnetism and for their technological applications. The magnetic properties of nanocrystals vary greatly with the changing size of the crystals and superparamagnetism is a typical example for such a size-dependent behaviour at the nanometre scale.[10] Among the wide variety of technological/medical applications, such as magnetic recording,[11] magnetic resonance

imaging, cell labelling, cell sorting agents,[12] *etc.*, each application requires a somewhat different set of magnetic characteristics in nanocrystals. Therefore, approaches such as preparing the ferrite oxides with uniform particle size are essential for controlling magnetic properties to satisfy the requirements in technical and biomedical applications of nanocrystals. Clearly, the systematic studies on the correlations between magnetic properties and the chemical compositions of nanocrystals will generate invaluable insight towards the fundamental understanding of magnetic properties, and consequently enable us to identify suitable candidates of magnetic nanocrystals for various applications.

Pristine and rare earth (RE) doped cobalt ferrites ($CoFe_2O_4$) belong to the crystal family of spinel ferrites. The magnetic properties of these oxides are mainly dominated by the distribution and the magnetic interaction among the cations in the two lattices, *i.e.*, tetrahedral (A) and octahedral (B). Because of the difference in the strengths of magnetic interactions at these 2 lattices of the spinel oxides, the magnetic properties possessed by doped $CoFe_2O_4$ nanocrystals vary with change in the cation distribution and therefore generate scope for the various applications. Cobalt ferrite can be represented as $(Co_x^{2+}Fe_{1-x}^{3+})$ $[Co_{1-x}^{2+}Fe_{1+x}^{3+}]O_4$, where x depends on the thermal history and the preparation condition. The systematic study of the significance of the method in the preparation of cobalt ferrite nanocrystals would provide insights for a better fundamental understanding of the correlations between the particle

Department of Chemistry, Goa University, Goa, 403206, India. E-mail: sal_arun@rediffmail.com; Fax: +91-832-2452889; Tel: +92-832-6519315

dimension, spin–orbit coupling and the magnetic properties. Consequently, the desirable magnetic properties for technological applications can be optimized through chemical changes which are sensitive to the preparation issues such as method, reaction conditions, particle size distribution and the occupancy of the different lattices by the metal ions, *etc.*

The sol–gel autocombustion method is one of the better methods and is widely used due to its effectiveness in obtaining the desired monophasic products with greater homogeneity and finer particle size at very low sintering temperatures. However to achieve the compositional homogeneity of the final oxide powder, the preparation of a homogeneous gel with respect to the distribution of cations is crucial. Therefore, it is essential to prepare a suitable precursor solution which can be converted to a gel without any cation segregation. For the first time we report the usage of malic acid and ethylene glycol as chelating and gelling agents at a neutral pH, for the sol–gel assisted autocombustion synthesis of doped cobalt ferrites of the type $CoFe_{2-x}RE_xO_4$ [($0 \leq x \leq 0.03$) and RE = Dy, Gd]. The significance of pH on the chelating action of the organic acid used, which is vital in preventing the precipitation and aggregation of the ions and maintaining the homogeneity of the mixture, has also been demonstrated. A detailed investigation on the influence of the distribution of the metal ions [Co^{2+}, RE^{3+} and Fe^{3+}] in the crystal lattice and the dimensions of the ferrite oxides on the resultant magnetic properties is reported here. The contribution of the spin–orbit coupling, generating from the Co^{2+} ions, towards higher magnetic anisotropy and hence the magnetic properties are also investigated. The results provide an insight into the inter-relationship of the particle dimension, the spin–orbit coupling and the resulting superparamagnetic property. Our conclusions on the structural and magnetic properties have been aptly supported by the magnetic and spectral data obtained from various characterization techniques employed, proving doped cobalt ferrite nanoparticles to be a suitable candidate in the technological and medical applications. We report a detailed investigation of the variation in the magnetic properties brought about with the introduction of the small doping concentration of Dy^{3+} and Gd^{3+} ions.

Experimental

Preparation

For the preparation of $CoFe_{2-x}RE_xO_4$ [($0 \leq x \leq 0.03$) and RE = Dy and Gd], stoichiometric amounts of analytical grade Co$(NO_3)_2 \cdot 6H_2O$ (Sigma-Aldrich), $Fe(NO_3)_3 \cdot 9H_2O$ (Sigma-Aldrich), Dy_2O_3 (Sigma-Aldrich) and Gd_2O_3 (Sigma-Aldrich) were utilised. To prepare Dy^{3+} doped cobalt ferrite, the water insoluble Dy_2O_3 was brought into solution form by dissolving it in concentrated AR-grade HNO_3 with vigorous stirring on a hot plate maintained at 100 °C. After obtaining a clear solution, Co$(NO_3)_2 \cdot 6H_2O$, $Fe(NO_3)_3 \cdot 9H_2O$ and double distilled water were added with continuous stirring. The required amount of malic acid (AR-grade) was then added. The pH of the solution was adjusted near neutral with the slow addition of 30% ammonia solution (AR-grade). A considerable change in colour from light pink to dark wine red was observed which confirmed the chelating action of malic acid. The dependence of chelating

action on pH seems to be very high as there was no chelation, and hence gel formation observed at lower pH values. The higher pH (near neutral) forces the organic acid to release the acidic proton and in turn chelates with the available metal ions. The pH of the solution was confirmed to be near neutral and then ethylene glycol in the ratio 1 : 4 (with respect to the malic acid) was added. The solution was then allowed to concentrate with continuous stirring. Once the formation of a highly viscous solution was observed, the beaker containing the contents was transferred to an oven and heated at a temperature of about 200 °C for 3 h. Formation of a voluminous foamy precursor was observed which was then crushed into fine powder with the help of an agate mortar and pestle. The precursor was then calcined at 400 °C for 4 h. It was again ground with acetone and then sintered at 600 °C for 6 h. The same procedure was utilised for the preparation of pristine and Gd^{3+} doped cobalt ferrite. The as obtained powder was then subjected to various characterisation techniques.

Characterization

The crystallinity, crystal structure and the phase purity of the powders were investigated by making use of the X-ray diffraction technique using Cu-K$_\alpha$ radiations of wavelength 1.5418 Å (filtered through Ni), in steps of 0.02 degrees on a RIGAKU ULTIMA IV X-ray diffractometer. The thermal behaviour of the gel and precursor was studied in dry air utilizing a NETZCH STA 409 PC TG/DTA instrument at a step rate of 10 °C min^{-1}. A SHIMADZU FTIR PRESTIGE-21 spectrophotometer was put into use to monitor the various changes taking place during the synthesis in the nature of the gel, the precursor and the oxide powders calcined at 400 °C and 600 °C. A comparative study of the Raman and IR active modes was done. Raman spectra were recorded in the backscattering geometry in the range 100–1000 cm^{-1} using a HORIBA JOBIN YVON HR-800 Raman spectrometer with an Olympus microscope (objective 50×) attachment and equipped with a CCD detector. A 488 nm Ar$^+$ ion laser with 10 mW power was used as the excitation source for a spot of about 1 mm in diameter. Particle size analysis of the as prepared nanoparticles was carried out at 25 °C by employing a DELSA NANO S, Beckman Coulter, USA. The morphology and the elemental analysis, using Energy Dispersive X-ray Spectroscopy (EDX) for the compounds, were carried out on a JEOL JSM-6360 LV Scanning Electron Microscope (SEM). Transmission Electron Microscopy (TEM) images were recorded on a PHILIPS CM 200 electron microscope, operating at an accelerating voltage of 200 kV and providing a resolution of 2.4 Å. The valence states and the binding energies of various chemical species were determined by the X-ray Photoelectron Spectroscopy (XPS) employing a VSW SCIENTIFIC INSTRUMENT with Al K$_\alpha$ as the incident source having an incident energy of 1486.6 eV with a resolution of 0.9 eV. The vacuum maintained in the sample analyzer chamber was 1.4×10^{-8} Torr. A QUANTUM DESIGN PPMS-VSM magnetometer was used for magnetic characterization of the pelletized compounds. The variation of the dc-susceptibility of each sample with temperature was measured from 5 K to 300 K in the ZFC (zero field cooling) and FC (field cooling) modes using a magnetic field of 10 kOe. The magnetization with varying magnetic field of up to 50 kOe was also measured at 5 K and 300 K.

This journal is © The Royal Society of Chemistry 2012

J. Mater. Chem., 2012, **22**, 2740–2750 | 2741

Results and discussion

Structural analysis

Fig. 1 shows the X-ray diffractograms of $CoFe_2O_4$ (CF), $CoFe_{1.97}Dy_{0.03}O_4$ (CDF) and $CoFe_{1.97}Gd_{0.03}O_4$ (CGF) sintered at 600 °C for 6 h. All the diffraction peaks observed for the oxides correspond to the spinel ferrite structure. The phase analysis was carried out by matching the obtained diffractograms with the standard ICDD card number 22-1086. The XRD pattern of the compounds reveal the monophasic formation of the poly-crystalline compounds. The X-ray diffractogram reveals the well crystalline nature of the compounds. An increase in the width of the XRD peaks with the inclusion of rare earth (RE^{3+}) ions is observed, which signifies that the compounds are constituted of finer particles. The broadening of the peaks also indicates the decrease in the density and an increase in the surface to volume ratio of the compounds with the doping of RE^{3+} ions. The unit cell parameter (a) calculated for pristine and doped cobalt ferrite as a Voigt function for the (311) peak shows an increase in the magnitude for the doped compounds, especially for the Dy^{3+} doped ferrite. Crystallite size and the lattice strain introduced with the doping are calculated from the X-ray diffractograms. Williamson–Hall extrapolations as a Lorentzian function are very well utilised in calculating these parameters for the pristine and doped compounds. Typical Williamson–Hall plots for CDF and CGF are displayed in Fig. 2. The results obtained on calculating the lattice parameters are presented in Table 1. One can observe from the results that the microdistortion value for the doped oxides is at least two times higher than that for the pristine cobalt ferrite. Dy^{3+} (1.05 Å) and Gd^{3+} (1.078 Å), being the larger cations as compared to the smaller sized Fe^{3+} (0.79 Å), cause the lattice expansion and this leads to an increase in the lattice strain.[13] The lattice parameters and the average particle size obtained with different RE^{3+} listed in Table 1 gives a fair idea of the changes brought about by the dopant in the cobalt ferrite lattice. A difference in these parameters was observed with the type of RE^{3+} ion doped. It is evident from the results obtained that the lattice parameters increase when doped with Dy^{3+}. The contribution of the larger ionic radius in the enhancement of these values is very significant. With the doping of Dy^{3+} ions with

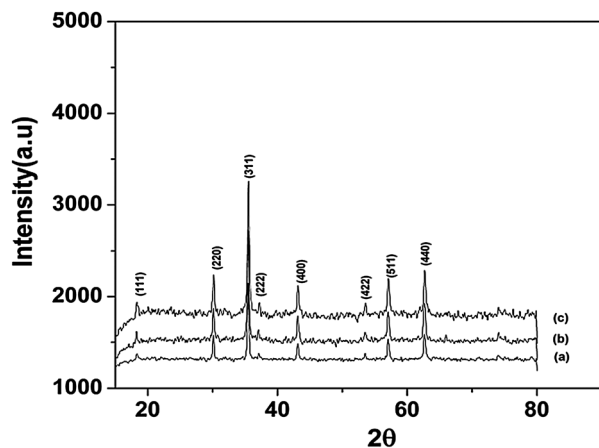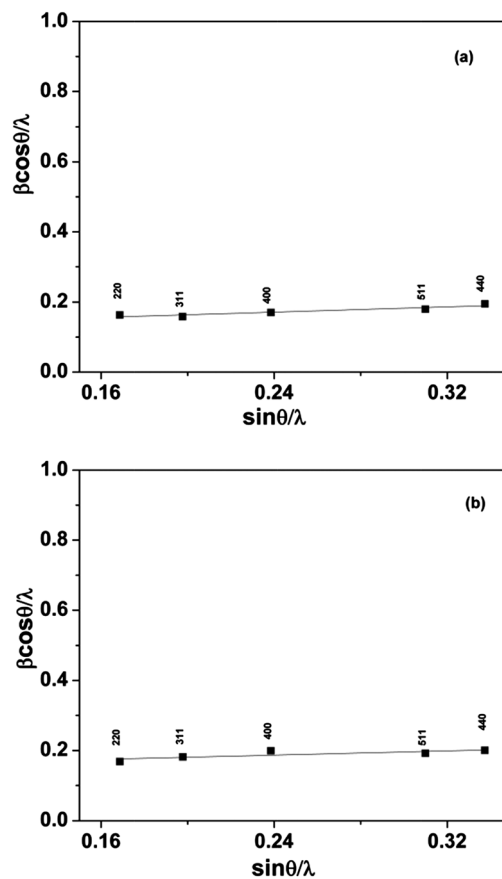**Fig. 2** Williamson–Hall plots of (a) CDF and (b) CGF.

larger ionic radii in the octahedral lattice (B), there is a reordering of cobalt ions from the octahedral lattice to the tetrahedral lattice (A). This process of ions changing their position from one lattice to another decreases the lattice strain that is induced by the doping and stabilises the structure. But there is a considerable difference in the values obtained with doping of Gd^{3+}. The results show a decrease in the lattice parameters. A similar decrease in the value of lattice parameters with the introduction of Sm^{3+} is reported.[14]

Infrared analysis

The FTIR spectra of the CDF gel (a), as-burnt (b) and calcined at 400 °C (c) and 600 °C (d) are presented in Fig. 3. From Fig. 3 (a), prominent peaks at 1382 and 833 cm^{-1} are assigned for the $(NO_3)^{-1}$ stretching frequency and in plane deformation frequency, and signals at 1587 and 1300 cm^{-1} (merged with the peak for nitrate) represent the asymmetric and symmetric stretching frequencies of the metal carboxylate linkages present in the gel matrix. A small peak in the region 1722 cm^{-1} is the signature peak for the ester carbonyl, signifying the presence of the ester linkages. The ester formation is a result of the condensation reaction between the –COOH of the malic acid and the –OH group coming from ethylene glycol in the provided pH condition (pH ≈ 6). A broad signal in the region 2500–3700 cm^{-1} represents N–H stretching (3400 cm^{-1}) and the O–H bonds (3000–3500 cm^{-1}) of glycol and water. Due to the merging of both the signals *i.e.*, for the –N–H bond and the –OH bond,

Fig. 1 XRD patterns of (a) CF, (b) CDF and (c) CGF sintered at 600 °C for 6 h.

Table 1 Dependence of lattice parameters on the type of RE^{3+} and comparison of the particle size obtained from XRD and particle size analyser

Composition	a/Å	Cell volume/m³	D_{XRD}/nm	$D_{Particle\ size\ analyser}$/nm	Strain (ε)
CF	8.3897	5.9052×10^{-28}	8	15	2.7×10^{-2}
CDF	8.3911	5.9082×10^{-28}	8	9	4.7×10^{-2}
CGF	8.3801	5.8850×10^{-28}	7	9	3.8×10^{-2}
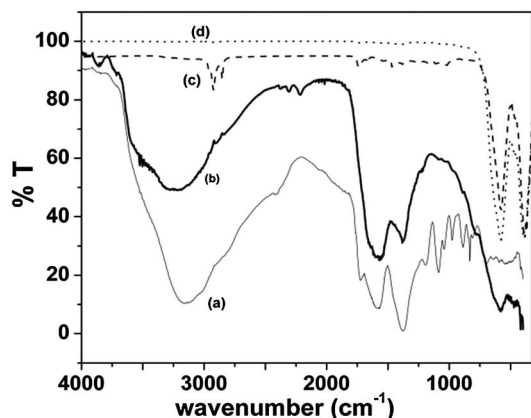
Fig. 3 FTIR spectra of CDF (a) gel, (b) as-burnt, (c) 400 °C and (d) 600 °C.

Fig. 4 TG–DTA curve of the CGF gel.

a common peak centering at 3145 cm^{-1} is observed. In addition another peak at 976 cm^{-1} is a representative peak for the O–H deformation along with a very weak signal at around 528 cm^{-1} assigned to the existence of OH bridges.[15] A band centred at 1087 cm^{-1} is evidence for the coordination of the alcoholic –OH group of the dibasic malate anion with the metal ion. The spectrum for the as-burnt precursor powder resultant of the combustion reaction is shown in Fig. 3(b). Disappearance of the signature peak for the ester linkages and a decrease in the intensity of the broad signal are the highlights of this spectrum. As mentioned, the heat of the combustion reaction is enough to cause the ester bonds to break resulting in the disappearance of the 1722 cm^{-1} signal. Apart from this, a peak with low intensity at 1382 cm^{-1} is also observed which reveals the presence of the $(NO_3)^{-1}$ ions trapped in the precursor matrix. As seen from Fig. 3(c), two prominent peaks centred at 574 and 385 cm^{-1} represent that of Fe–O stretching in the tetrahedral and octahedral lattices. The position of the tetrahedral peak in the FTIR spectra is at a higher region as compared to that of the octahedral peak. The Fe–O bond in the tetrahedral lattice has a shorter bond length as compared to that in the octahedral lattice and therefore more energy is required to vibrate the bond. There is a shift in the position of the Fe–O octahedral stretching peak from 385 to 393 cm^{-1}, accompanied with an increase in its intensity as seen from Fig. 3(d). This figure represents the compound sintered at 600 °C with almost an equal distribution of the Fe^{3+} ions in both the lattices.

Thermal analysis

Fig. 4 portrays the TG–DTA curve of the CDF gel carried out in air from 28 °C to 1000 °C at a heating rate of 10 °C min^{-1}. The
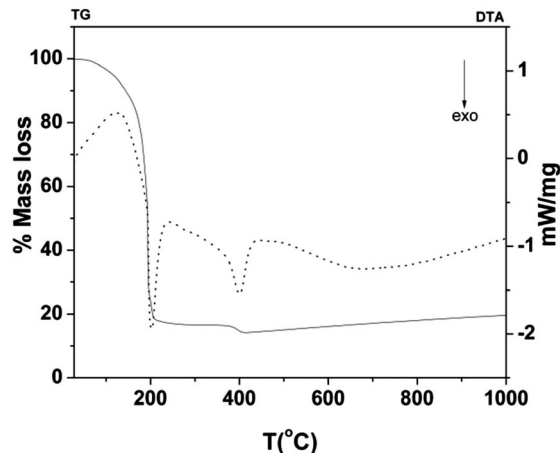
molecular formula for the iron cobalt malate complex can be given as $[Fe_2Co(C_4H_4O_5)_2(OH)_4] \cdot 6H_2O$.[15] It is very much similar to the CDF gel except for the partial substitution of RE^{3+} and the usage of ethylene glycol as a gelling agent. V. Buzko *et al.* report on the complex formation of RE^{3+} ions with malic acid,[16] so the overall formula of the complex with the inclusion of RE^{3+} ions can be written as $[Fe_{2-x}RE_xCo(C_4H_4O_5)_2(OH)_4] \cdot 6H_2O$. Since it is very difficult to estimate the ethylene glycol concentration, it is not mentioned in the coordination sphere. The curve for CDF can be divided into four regions with various processes taking place in each region *i.e.*, (i) 28–150 °C, (ii) 150–300 °C, (iii) 300–480 °C and (iv) 480–1000 °C. In the first region there is an endothermic reaction witnessed at 135 °C for the dehydration process associated with a mass loss of 20%. An exothermic process at 207 °C is associated with a high mass loss of 54%.

This is a combustion reaction which involves the oxidative decomposition of the gel along with the evolution of NH_3, NO_3^{-1} and CO_2. In the third region another exotherm at 421 °C is observed with a mass loss of 12%. This may be associated with the oxidation of the residual carbon which is evident even in the fourth region of the curve.
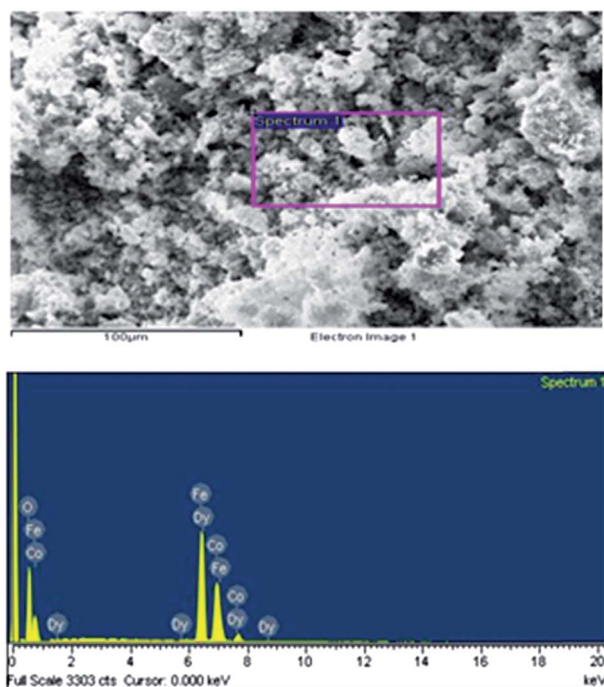
Morphology and chemical analysis

The scanning electron micrographs of CDF and CGF sintered at 600 °C are presented in Fig. 5. The images display a flaky and porous morphology for all the oxide ferrite samples *i.e.*, CDF and CGF. The micrographs display the formation of secondary particles or large lumps of aggregates which may be due to the agglomeration of the primary particles. A consistency in the ferrite phase formation is obvious for all the samples. The chemical analysis data obtained from EDX also confirm the

This journal is © The Royal Society of Chemistry 2012

J. Mater. Chem., 2012, **22**, 2740–2750 | 2743
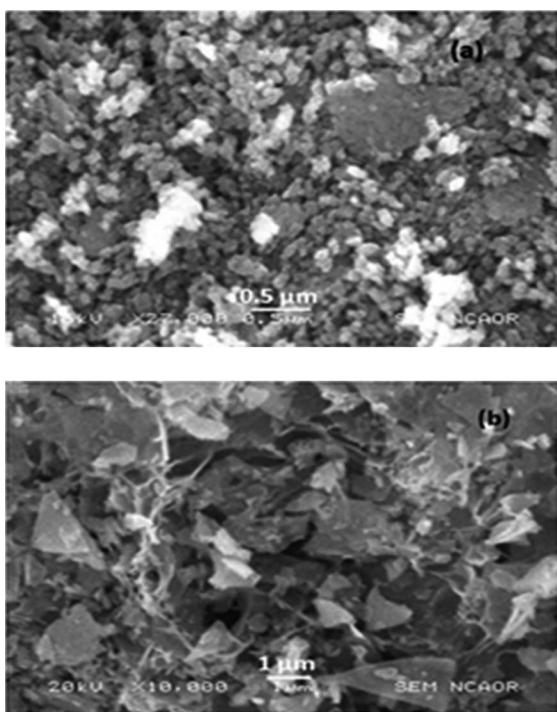
Fig. 5 SEM micrographs of (a) CDF and (b) CGF.

metal ion ratios to match with that of the single phase ferrite which is equally backed up by the X-ray diffraction results. The elemental analysis results of CDF are displayed in Fig. 6. This shows a complete agreement of the observed percentage of the metal ion with that of the calculated one. The obtained ferrite sample is free from residual carbon which can be confirmed from

the full scan XPS data for the ferrite. The results obtained for the elemental analysis are presented in Table 2.

Particle size analysis

Particle size analysis of CDF and CGF calcined at 600 °C reveals the average particle diameter of the compounds. As a representative figure, the differential intensity *versus* particle size distribution of CDF and CGF obtained from particle size analysis study at 25 °C is shown in Fig. 7(a) and (b). The Lorentzian distribution function revealed the average particle size to be 10 nm and 9 nm for CDF and CGF samples respectively.

The TEM images of CDF and CGF along with their electron diffraction pattern are represented in Fig. 8(a) and (b). The images reveal the particles to be hexagonal in nature, partially agglomerated with uniform particle size which can be correlated with the results obtained from the particle size analyser. There is uniformity in the particle diameter as observed from the TEM images with smaller particle size. When doped in cobalt ferrites, the RE^{3+} ions segregated closer to the grain boundaries thereby minimising the possibility of increasing the grain size by the process of agglomeration. The well crystallised nature of Dy^{3+}

Table 2 Percentage of the elements, calculated and as obtained from the EDX analysis

	% Fe	% Co	% Dy	% O
Calculated percentage	46.26	24.78	2.05	26.91
Observed percentage	44.53	28.13	2.24	25.09

Fig. 6 Elemental analysis by EDX.
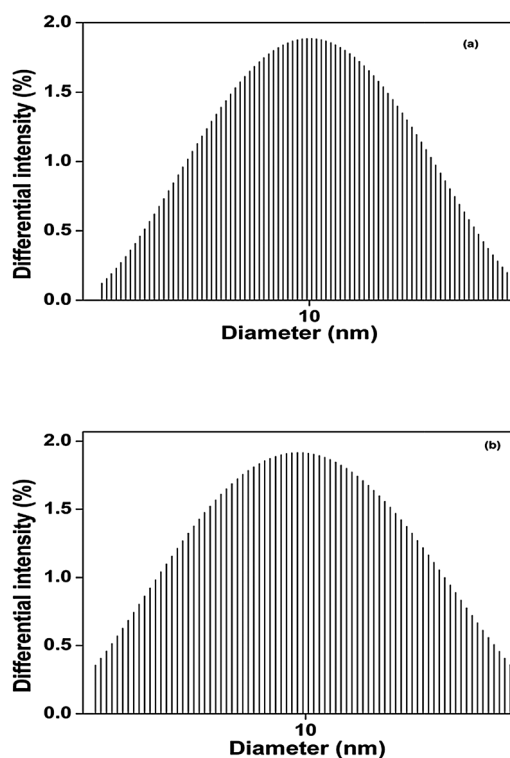
Fig. 7 Grain size histograms obtained by the statistical method: (a) CDF and (b) CGF.
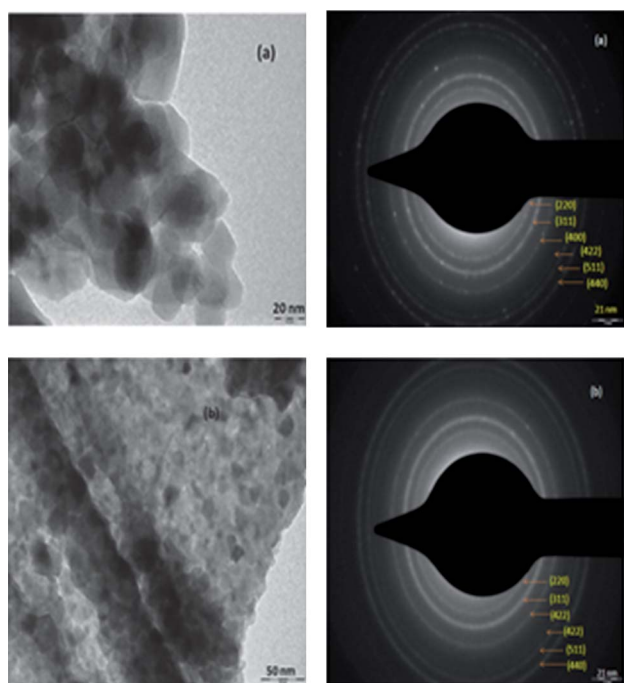
Fig. 8 TEM images of (a) CDF and (b) CGF sintered at 600 °C.

Fig. 9 Raman spectra of (a) CF, (b) CDF and (c) CGF sintered at 600 °C.

Fig. 10 The deconvulated pattern (a and b) and a short range comparative study of Raman and FTIR active modes for CDF carried out at room temperature shown in (c).

cobalt ferrite is very much obvious from the electron diffraction pattern from which the position of the individual planes for the spinel cobalt ferrite can be clearly designated. With the doping of Gd^{3+} there is a decrease in the crystalline nature which can be clearly seen from the increase in the peak width of the X-ray diffractograms and also from the electron diffraction patterns. Since a lot of energy is required to push the RE^{3+} ions with high ionic radii in place of Fe^{3+} and form the RE–O bond, the energy supplied is utilised for this process at the expense of crystallisation and therefore the decrease in crystalline nature with smaller particle size is observed. Similar decrease in crystallinity is reported by L. Zhao et al.[17] for the inclusion of Nd^{3+} in cobalt ferrite.

Raman spectroscopy

Raman spectroscopy is a highly sensitive tool for many lattice effects, such as structure transition, lattice distortion, charge–lattice and spin–lattice couplings, local cation distribution, and magnetic ordering. Doped cobalt ferrite has a cubic mixed ferrite structure with O^7_h ($Fd3m$) space group which gives rise to 39 normal modes, out of which five are Raman active. The room-temperature Raman spectrum of doped cobalt ferrite nanoparticles in the region 100–1000 cm^{-1} is presented in Fig. 9(a). The spectrum reveals the single phase formation of the polycrystalline compound. All the 5 ($1A_{1g} + 1E_g + 3T_{2g}$, Raman active modes which are expected for the cubic spinel ferrite system) are visible in the spectrum. The deconvulated spectra (using suitable peak fitting software) reveal the presence of 7 peaks in the Raman spectra at 308 cm^{-1}, 357 cm^{-1}, 469 cm^{-1}, 577 cm^{-1}, 617 cm^{-1}, 658 cm^{-1} and 693 cm^{-1}, most of which are the typical modes of the cubic inverse-spinel ferrite structure represented in Fig. 10(a) and (b). The T_{2g} mode expected at ~190 cm^{-1}
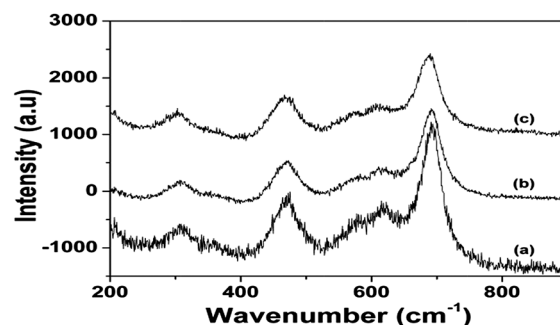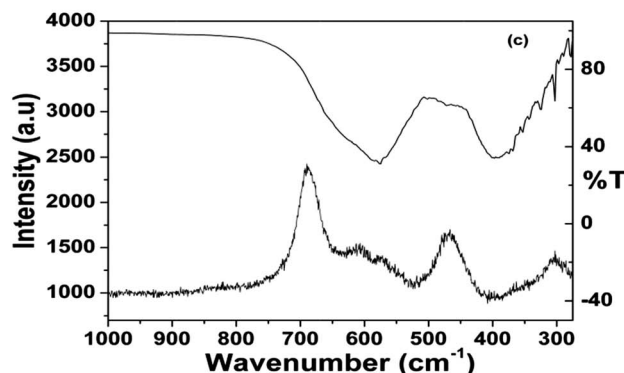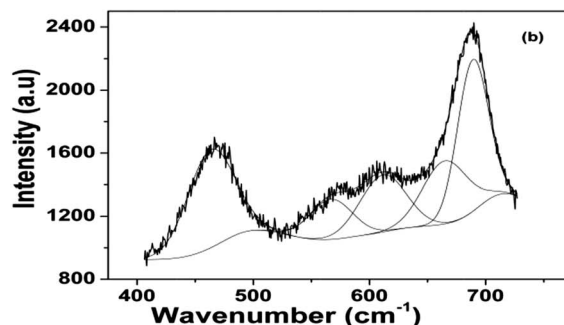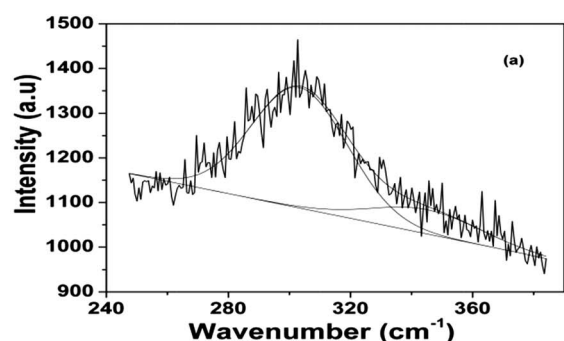
for the compound is not clear from the spectra, but we do observe a peak at 308 cm^{-1} which can be attributed to the E_g mode.[18] The Raman peak at 469 cm^{-1} reflects the local lattice

This journal is © The Royal Society of Chemistry 2012

J. Mater. Chem., 2012, 22, 2740–2750 | 2745

effect in the octahedral sublattice of $CoFe_2O_4$ [ref]. The other intense peak at 693 cm^{-1} and a small peak at 617 cm^{-1} (the A_{1g} mode) are the symmetry vibrations of the metal in the tetrahedral site.[18] A peak is observed in the region of 658 cm^{-1} which can be attributed to cobalt ions residing at defect sites that are probably located near the surface of the nanoparticles.[18] This peak is particularly pronounced due to the higher surface-to-volume ratio of the nanoparticles in this sample. Fe_2O_3 is the most common impurity phase formed during the synthesis of spinel ferrites. It gives two sharp signals at ∼240 and 300 cm^{-1} with high intensity. The 240 cm^{-1} peak is absent in the spectrum and a protrusion is observed at 308 cm^{-1}. This is comparatively mild in intensity and can therefore be said to be the property of cobalt ferrite and not Fe_2O_3. Similarly no individual oxide peaks for the dopants are observed confirming the compound to be of monophasic composition. All together there are two different lattices in the spinel ferrites structure, and an attempt is made here to assign the modes for the various signals observed in the spectra based on the idea obtained from the literature.[8,18–23]

The vibrational modes in the Infra Red (IR) spectroscopy for a compound are different from the ones observed in Raman spectroscopy. We show the difference between the Raman and IR vibrational modes for cobalt ferrite in Fig. 10. There are 4 different modes (ν_1, ν_2, ν_3 and ν_4) assigned to the tetrahedral lattice. All the 4 modes are Raman active while only 2 (ν_3 and ν_4) are IR active. From the figure, the asymmetric IR stretching (T_1) modes are evident for the compound at 400 and 572 cm^{-1}, which can be correlated with the Fe–O stretching in the octahedral and the tetrahedral lattice, along with the other 2 signals at 279 and 302 cm^{-1}. In contrast the signal evident at 400 cm^{-1} for the octahedral site which is highly intense in the IR region is absent in the Raman spectra proving it to be either a ν_3 or a ν_4 mode which are strong IR active modes and poor in the Raman spectra. We could observe a weakly intense signal in the Raman spectra as compared to that of the IR signal at 572 cm^{-1} (for tetrahedral Fe–O stretching) which makes us infer that ν_3 and ν_4 must be strong IR active modes only, and the modes observed in the Raman spectrum can be the ν_1, ν_2 (tetrahedral) and the ν_1, ν_2 and the ν_5 modes (octahedral lattice) and very weak ν_3 and ν_4 modes.

XPS analysis

X-Ray photoelectron spectroscopy (XPS) is a powerful tool in determining the oxidation states and the binding energy of the various chemical species present in a compound. A change in the oxidation state brings along a change in the arrangement of electrons and thereby changing the properties of a system. The spectra of all the elements along with the full scan are plotted and deconvulated using peak fitting software. The spectra of the full scan (FS) for CDF and CGF are presented in Fig. 11(a) and (b). From the FS spectrum, we can clearly observe the respective peaks for O 1s, Fe 2p, Co 2p, Dy 3d and Gd 3d which confirms the elements to be present in the system. We could verify the absence of carbon in the material based on the absence of the carbon peak which normally originates at 285 eV. The valence state of iron and cobalt decides the overall magnetic moment of the system. The overall preparation is carried out in an oxygen rich atmosphere and therefore there is a possibility of redox
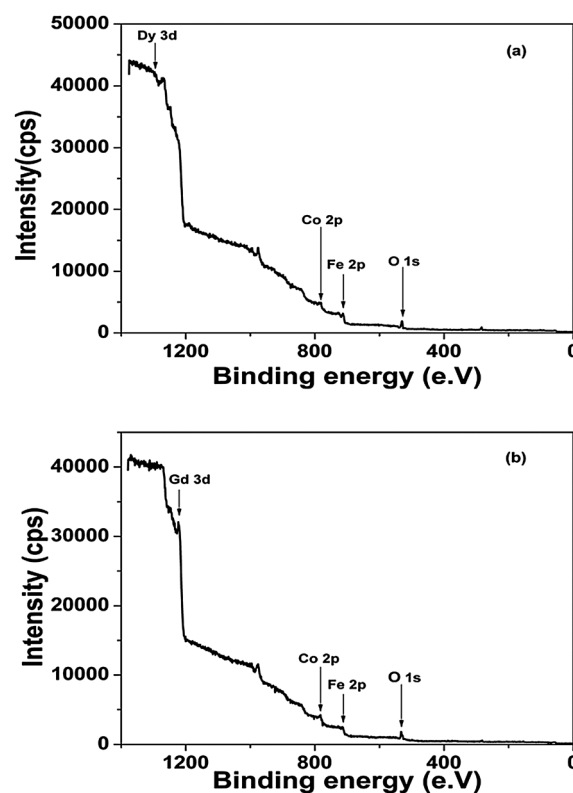

Fig. 11 Full scan XPS spectra displaying the chemical composition of (a) CDF and (b) CGF.

reaction to occur in which electron exchange can take place between Co^{2+} and Fe^{3+} to form Fe^{2+} and Co^{3+} ions, thereby reducing the overall magnetic moment. The XPS spectrum of Fe 2p is presented in Fig. 12(a). The spectrum reflects two signals at 725.46 and 711.94 eV. These peaks represent the Fe $2p_{1/2}$ and Fe $2p_{3/2}$ for the Fe^{3+} state, confirming the valence state of iron to be Fe^{3+} and not Fe^{2+} and also ruling out the possibility of metal Fe. The corresponding spectrum for Co 2p is presented in Fig. 12(b). From the figure, the signals for Co $2p_{1/2}$ and Co $2p_{3/2}$ are observed at 795 and 779 eV respectively which are characteristic binding energies for the Co^{2+} state. The spectra representing the Dy^{3+} and Gd^{3+} binding energies for the 4s and 4p states are shown in Fig. 11(c) and (d). The peaks representing the Dy 4s, Dy $4p_{1/2}$ and Dy $4p_{3/2}$ for the Dy^{3+} state are seen at 413, 338 and 299 eV. The signals for the Gd 4s, Gd $4p_{1/2}$ and Gd $4p_{3/2}$ for the Gd^{3+} state are seen at 368, 299 and 275 eV respectively. The binding energy of the oxygen species corresponding to the O 1s is presented in Fig. 12(e). The value obtained for the binding energy (531.7 eV) is in compliance with the standard. Our studies confirm the existence of the metal ions in the required valency thereby contributing positively towards the overall magnetic moment.

Magnetic measurements

The ZFC and FC susceptibility *versus* temperature curves of the $CoFe_{2-x}RE_xO_4$ ($x = 0.0$, 0.03, RE = Dy, Gd) nanoparticles are shown in Fig. 13. A net irreversibility is observed between the ZFC and FC curves for all the samples *i.e.*, the ZFC curve shows
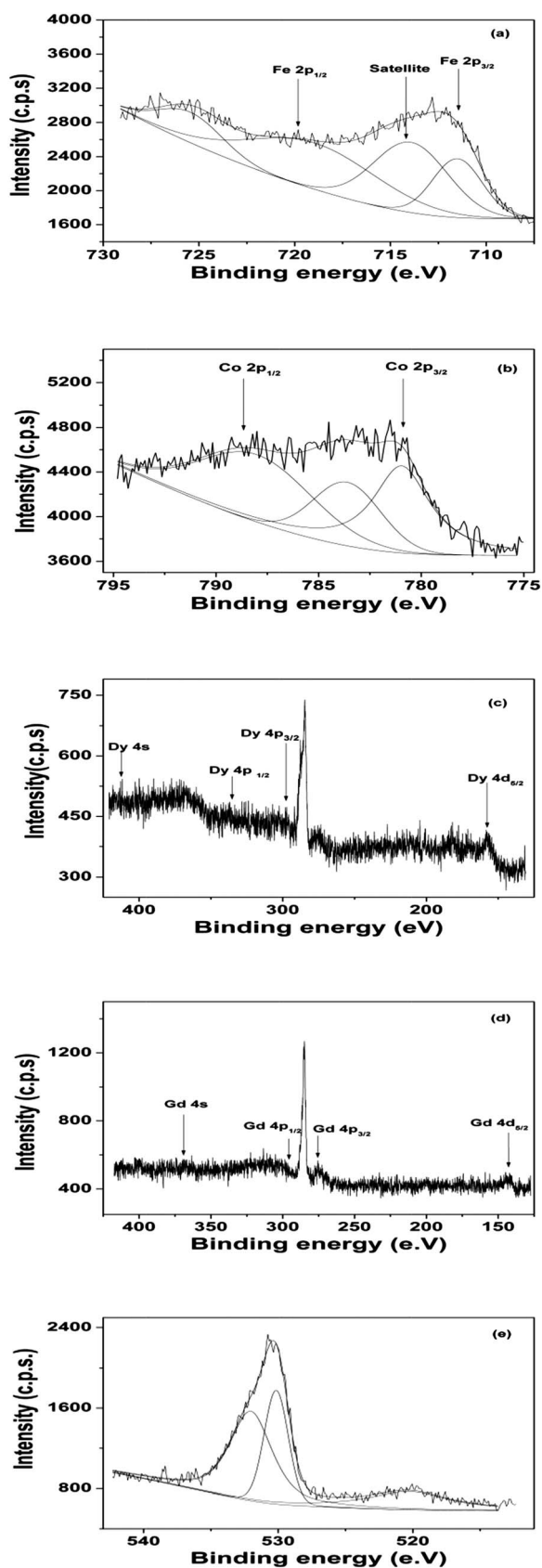
Fig. 12 XPS spectra displaying the binding energy and chemical states of (a) Fe 2p, (b) Co 2p, (c) Dy, (d) Gd and (e) O 1s.
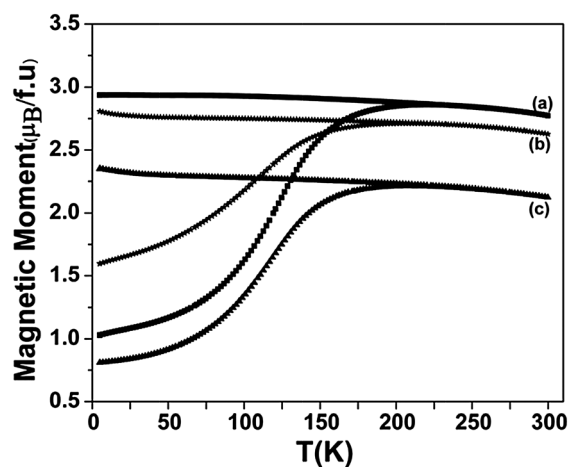

Fig. 13 M–T behaviour of (a) CF, (b) CDF and (c) CGF at a magnetic field of 1 Tesla.

a clear maximum at a critical temperature and decreases rapidly to zero with decrease in the temperature, while FC remains almost constant below this critical temperature, which is typical of a superparamagnetic state. The as-obtained nanoparticles can therefore be considered as magnetic single domains with a blocking temperature (T_B) corresponding to the maximum value of the ZFC curve. T_B is known as the temperature at which the magnetic anisotropy energy barrier of a nanomagnet is overcome by thermal activation, leading to the fluctuation of its magnetization.[24] Surprisingly, the T_B values for the substituted ferrite samples are smaller by about 6–10 K than that of CF. As reported, the Néel theory explains the dependency of the blocking temperature on K (the magnetocrystalline anisotropy constant), and/or V (the average particle volume) and is related with the help of the equation[25]

$$25k_B T_B = KV \qquad (1)$$

In the present case, the particle size decreases with RE substitution which leads to a decrease in the average particle volume. T_B decreases with RE substitution, irrespective of the nature of the RE^{3+} ion, suggesting that the contributions of V and a probable cation disorder towards the lowering of T_B are significant. It is well known that $CoFe_2O_4$ exhibits an inverse-spinel structure, where Co^{2+} ions are exclusively octahedrally coordinated, while Fe^{3+} ions are both tetrahedrally and octahedrally coordinated.[26,27] Prepared by wet chemical routes, cobalt ferrite can depart from the thermodynamically stable structure and can be described by the appropriate formula as $(Co_\lambda^{2+}Fe_{1-\lambda}^{3+})$ $[Co_{1-\lambda}^{2+}Fe_{1+\lambda}^{3+}]O_4$, where parentheses and square brackets correspond to the tetrahedral and octahedral lattices of the spinel structure, respectively. The degree of structure inversion is measured by $\lambda < 1$. For instance, λ is found to be about 0.4 and 0.84 in 8 nm and 5.5 nm CF particles, respectively, prepared by coprecipitation method[8] and the polyol method.[11] It is estimated to be about 0.69 and 0.8 in 20 nm and 5 nm sized particles prepared by micellar technique.[28,29] The 20, 40, 70 and 100 nm sized particles obtained by the mediated growth dominant coprecipitation and modified oxidation method report the degree

This journal is © The Royal Society of Chemistry 2012

J. Mater. Chem., 2012, 22, 2740–2750 | 2747

of inversion to be 0.75 which is independent of the particle size obtained.[30] In all cases, the magnetic properties appear to be sensitive to the cation distribution between the octahedral and tetrahedral sites. Moreover, the entrance of RE^{3+} ions of large radii into the octahedral lattice sites (the most probable) of the spinel lattice could induce some rearrangement. Indeed, it is reported that the original distribution of the cations in the octahedral and tetrahedral spinel sites may be drastically influenced by the substitution of other ions,[31,32] so doping with the RE^{3+} ions probably destroys the original distribution equilibrium thereby transferring the Co^{2+} ions to the tetrahedral site. It is a selective transfer of Co^{2+} ions as compared to the Fe^{3+} ions, because the Co^{2+} ions (0.745 Å) are bigger than Fe^{3+} ions (0.645 Å). Probably, a certain number of these cations should migrate from the octahedral sites to the tetrahedral ones, accompanied by a reverse transfer of Fe^{3+} ions from the tetrahedral to the octahedral ones in order to relax the strain introduced by RE substitution. The population of Co^{2+} cations in the octahedral spinel sites decreases, which affects the magnetic properties of the RE-substituted ferrites by lowering the single ion anisotropy of the Co^{2+} ions present in the crystal lattice and thereby lowering the T_B value. Mossbauer spectroscopy can be employed to confirm the structural deviation from an inverse-spinel-like lattice of the particles reported herein. Fig. 14 represents the dependence of the magnetization (M) on the magnetic field (H) of pristine and doped cobalt ferrite nanoparticles at (a) 300 K and (b) 5 K. Beyond T_B,
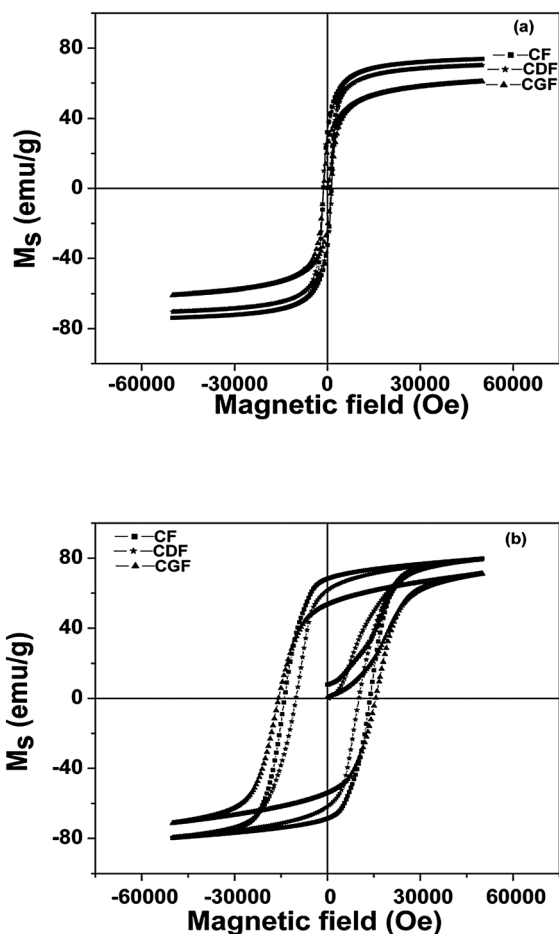
neither the remanance nor coercivity and therefore none of the hysteresis features are in agreement with the superparamagnetic character of the particles. Beyond T_B, these nanoparticles exhibit ferrimagnetic behaviour characterized by hysteresis loops with coercivity, remanance and saturation magnetization. All these observations are listed in Table 3. There is a considerable difference in the magnetic properties observed at 5 K. The increase in these values may be because of the proper ordering of the magnetic moments along the direction of the magnetic field which in turn is disturbed at elevated temperatures (at 300 K) due to the randomisation of the magnetic moment by the thermal vibrations. The variation of magnetization *versus* magnetic field (H) at 5 K of CF, CDF and CGF is plotted in Fig. 14(b). Hysteresis is observed with a large coercivity and saturation magnetization. It is observed that the value of saturation magnetization (M_s) decreases with the RE^{3+} inclusion. This decrease could be mainly correlated with the decrease in particle size brought about with the doping. Theoretically an increase in the magnetic properties should be expected as the magnetic moment of Gd^{3+} ($4f^7$) and Dy^{3+} ($4f^9$) residing in octahedral sites is higher as compared to that of Fe^{3+} ($3d^5$). This can also be due to the relatively important migration of Co^{2+} ($3d^7$) ions from the octahedral to the tetrahedral sites with a magnetic moment aligned antiparallel to those of RE^{3+} ions in the spinel lattice. Therefore the overall magnetic moment should show a decrease when doped with the RE^{3+} ions. But due to the variation in the particle sizes of CDF and CGF as compared to that of CF it becomes difficult to gauge the positivity in magnetic properties practically. In addition, the higher magnetic moment of the Dy^{3+} ions (10.74 BM) as compared to that of the Gd^{3+} (9.64 BM) results in the higher values of the magnetic properties. The higher magnetic moment of Dy^{3+} ions masks the ability of the Gd^{3+} ions (with higher ionic radius) to enhance the migration of Co^{2+} to the tetrahedral site, thereby increasing the saturation magnetisation. Therefore the saturation magnetisation of CGF is lower than that of CDF, suggesting that the ionic radii may not be the only deciding factor that influences drastically the inversion rate of Co^{2+}, thereby influencing the magnetic properties. The remanance (M_r), the saturation magnetisation (M_s) and the coercivity (H_c) at 5 K and 300 K are given in Table 3. The coercivity varies with RE^{3+} ion type. It is low for CDF as compared to that of pristine cobalt ferrite particles but the CGF sample shows values higher than pristine and CDF. The Dy^{3+} and Gd^{3+} ions have no orbital contribution to the magnetic interaction. The observed loss of magnetocrystalline anisotropy, through the drop in the H_c value, is related to a probable migration of Co^{2+} ions from octahedral to tetrahedral sites. The

Fig. 14 M–H behaviour of the compounds at (a) 300 K and (b) 5 K.

Table 3 Magnetic characteristics of the $CoFe_{2-x}RE_xO_4$ ($x = 0.0, 0.03$, RE = Dy, Gd) nanoparticles at 300 K and 5 K

Temperature/K	Saturation magnetisation (M_s)/emu g^{-1}	Coercivity (H_c)/kOe	Remanance (M_r)/emu g^{-1}	M_r/M_s
CF (300 K)	73.84	1.326	32.8	0.44
CF (5 K)	79.69	13.939	68.3	0.86
CDF (300 K)	70.29	1.435	33.3	0.47
CDF (5 K)	79.35	10.149	61.67	0.78
CGF (300 K)	60.85	1.215	22.5	0.37
CGF (5 K)	71.02	15.602	53.5	0.75

change in the magnetocrystalline anisotropy that is brought about with this probable transfer can be explained as follows. The magnetocrystalline anisotropy energy, E_A, of a single domain nanocrystal is approximated by

$$E_A = KV\sin^2\theta \qquad (2)$$

where K is the magnetocrystalline anisotropy constant, V is the volume of nanocrystal, and θ is the angle between the easy axis of nanocrystal and the direction of field-induced magnetization.[33] For a crystal with a cubic spinel structure, metal cations occupy the tetrahedral (A) and octahedral (B) lattice sites. Since the ligand field is weak in spinel ferrites, all cations assume high spin states. A Fe^{3+} cation with $3d^5$ electron configuration usually has its orbital angular momentum quenched in a weak ligand field. Therefore, the contribution to the magnetic anisotropy should only come from Co^{2+} cations in CF. The L–S coupling strength of the Co^{2+} determines the relative magnitude of magnetic anisotropy. The cubic symmetry in spinels is often lowered to a trigonal field due to the structural distortion from the Jahn–Teller effect and/or the nonstructural distortion from the interactions between the central cation and the cations outside the nearest neighborhood of the central ion. A Co^{2+} cation in CF with $3d^7$ electron configuration at a B site has a triplet $^4T_{1g}$ ground state. Even though the trigonal field is introduced with the T_{1g} ground state further splitting into A_2 and E states, the Co^{2+} cation with a degenerated ground state of E is still considered to have a strong L–S coupling, and consequently contributes greatly to the magnetic anisotropy of CF.[34,35] The strong L–S couplings at Co^{2+} lattice sites surely will generate a large anisotropy constant K and result in much higher anisotropy energy barriers in CF nanocrystals. Hence, we observe higher blocking temperature for CF nanocrystals than the doped ferrites. The anticipated magnetic anisotropy increase with RE substitution in CF particles appears here as quite compromised. In all evidence, the coercivity of the CDF and CGF particles prepared by the sol–gel autocombustion method does not only depend on the single-ion anisotropy of RE^{3+} cations but also on the effective Co^{2+} ion transfer that is brought about by the doping of RE^{3+} ions and the size of the particles. The lattice distortion of these spinels and the probable Co^{2+} transfer to the tetrahedral sites contribute strongly in the variation observed in H_c and, in a similar way, T_B.

Conclusion

The monophasic preparation of the doped cobalt ferrite nanocrystalline compound was carried out successfully by the sol–gel autocombustion method. The structural characterization proved the monophasic formation and confirmed the nanocrystalline nature of the particles. The Raman spectroscopy effectively demonstrated the formation of the spinel phase only, thereby eliminating the probability of the formation of the α-Fe_2O_3 phase. The X-ray Photoelectron Spectroscopy (XPS) confirmed the presence of the metal ions in the required valence state, thereby contributing effectively towards the overall magnetic moment. We could successfully demonstrate the large variation in the magnetic properties displayed by the material with varying field and also at different temperatures. It can be concluded that

the strong L–S coupling from the Co^{2+} ions in the octahedral lattice is a deciding factor in the display of blocking temperature for the individual compounds. The lattice distortion of the doped ferrites and a probable Co^{2+} transfer from the octahedral to the tetrahedral site play a vital role in deciding the overall magnetic properties displayed by the materials.

References

1 Q. Song and Z. J. Zhang, *J. Am. Chem. Soc.*, 2004, **126**, 6164–6165.
2 L. D. Tung, V. Kolesnichenko, D. Caruntu, N. H. Chou, C. J. O'Connor and L. Spinu, *J. Appl. Phys.*, 2003, **93**, 7486–7488.
3 T. Hyeon, Y. Chung, J. Park, S. S. Lee, Y.-W. Kim and B. H. Park, *J. Phys. Chem. B*, 2002, **106**, 6831–6833.
4 R. S. Devan, Y. D. Kolekar and B. K. Chougule, *J. Phys.: Condens. Matter*, 2006, **18**, 9809–9821.
5 N. Sivakumar, A. Narayanasamy, K. Shinoda, C. N. Chinnasamy, B. Jeyadevan and J.-M. Greneche, *J. Appl. Phys.*, 2007, **102**, 0139161–0139168.
6 B. X. Gu, *Appl. Phys. Lett.*, 2003, **82**, 3708–3709.
7 F. Cheng, C. Liao, J. Kuang, Z. Xu, C. Yan, L. Chen, H. Zhao and Z. Liu, *J. Appl. Phys.*, 1999, **85**, 2782–2786.
8 M. A. G. Soler, E. C. D. Lima, S. W. da Silva, T. F. O. Melo, A. C. M. Pimenta, J. P. Sinnecker, R. B. Azevedo, V. K. Garg, A. C. Oliveira, M. A. Novak and P. C. Morais, *Langmuir*, 2007, **23**, 9611–9617.
9 N. Moumen and M. P. Pileni, *Chem. Mater.*, 1996, **8**, 1128–1134.
10 E. Manova, B. Kunev, D. Paneva, I. Mitov, L. Petrov, C. Estournés, C. D'Orléans, J.-L. Rehspringer and M. Kurmoo, *Chem. Mater.*, 2004, **16**, 5689–5696.
11 S. Ammar, A. Helfen, N. Jouini, F. Fiévet, I. Rosenman, F. Villain, P. Molinié and M. Danot, *J. Mater. Chem.*, 2001, **11**, 186–192.
12 E. V. Groman, J. C. Bouchard, C. P. Reinhardt and D. E. Vaccaro, *Bioconjugate Chem.*, 2007, **18**, 1763–1771.
13 L. B. Tahar, L. S. Smiri, M. Artus, A.-L. Joudrier, F. Herbst, M. J. Vaulay, S. Ammar and F. Fiévet, *Mater. Res. Bull.*, 2007, **42**, 1888–1896.
14 M. M. Rashad, R. M. Mohamed and H. El-Shall, *J. Mater. Process. Technol.*, 2008, **198**, 139–146.
15 T. V. Albu, I. Mindru, L. Patron, E. Segal and M. Brezeanu, *Thermochim. Acta*, 1999, **340–341**, 235–240.
16 V. Buzko, I. Sukhno and V. Klimova, *Acta Chim. Slov.*, 2004, **51**, 213–222.
17 L. Zhao, H. Yang, X. Zhao, L. Yu, Y. Cui and S. Feng, *Mater. Lett.*, 2006, **60**, 1–6.
18 G. Shemer, E. Tirosh, T. Livneh and G. Markovich, *J. Phys. Chem. C*, 2007, **111**, 14334–14338.
19 T. Yu, Z. X. Shen, Y. Shi and J. Ding, *J. Phys.: Condens. Matter*, 2002, **14**, L613–L618.
20 S. Ayyappan, S. Mahadevan, P. Chandramohan, M. P. Srinivasan, J. Philip and B. Raj, *J. Phys. Chem. C*, 2010, **114**, 6334–6341.
21 L. Li, *J. Sol-Gel Sci. Technol.*, 2011, **58**, 677–681.
22 M. A. G. Soler, T. F. O. Melo, S. W. da Silva, E. C. D. Lima, A. C. M. Pimenta, V. K. Garg, A. C. Oliveira and P. C. Morais, *J. Magn. Magn. Mater.*, 2004, **272–276**, 2357–2358.
23 F. Nakagomi, S. W. da Silva, V. K. Garg, A. C. Oliveira, P. C. Morais, A. Franco Júnior and E. C. D. Lima, *J. Appl. Phys.*, 2007, **101**, 09M5141–09M5143.

This journal is © The Royal Society of Chemistry 2012

J. Mater. Chem., 2012, **22**, 2740–2750 | 2749

24 F. J. Owens and C. P. Poole, Jr, *The Physics and Chemistry of Nanosolids*, John Wiley and Sons, Inc., New Jersy, 2008.

25 X. M. Lin, C. M. Sorensen, K. J. Klabunde and G. C. Hadjipanayis, *Langmuir*, 1998, **14**, 7140–7146.

26 K. E. Mooney, J. A. Nelson and M. J. Wagner, *Chem. Mater.*, 2004, **16**, 3155–3161.

27 M. Veverka, P. Veverka, O. Kaman, A. Lančok, K. Závĕta, E. Pollert, K. Knížek, J. Boháček, M. Beneš, P. Kašpar, E. Duguet and S. Vasseur, *Nanotechnology*, 2007, **18**, 3457041–3457047.

28 C. Liu, B. Zou, A. J. Rondinone and Z. J. Zhang, *J. Am. Chem. Soc.*, 2000, **122**, 6263–6267.

29 N. Moumen, P. Bonville and M. P. Pileni, *J. Phys. Chem.*, 1996, **100**, 14410–14416.

30 C. N. Chinnasamy, B. Jeyadevan, K. Shinoda, K. Tohji, D. J. Djayaprawira, M. Takahashi, R. J. Joseyphus and A. Narayanasamy, *Appl. Phys. Lett.*, 2003, **83**, 2862–2864.

31 L. B. Tahar, M. Artus, S. Ammar, L. S. Smiri, F. Herbst, M.-J. Vaulay, V. Richard, J.-M. Grenéche, F. Villain and F. Fiévet, *J. Magn. Magn. Mater.*, 2008, **320**, 3242–3250.

32 X. Meng, H. Li, J. Chen, L. Mei, K. Wang and X. Li, *J. Magn. Magn. Mater.*, 2009, **321**, 1155–1158.

33 C. R. Vestal and Z. John Zhang, *Nano Lett.*, 2003, **3**, 1739–1743.

34 C. Liu, B. Zou, A. J. Rondinone and Z. J. Zhang, *J. Am. Chem. Soc.*, 2000, **122**, 6263–6267.

35 J. E. Huhey, E. Kieter and R. Kieter, *Inorganic Chemistry: Principles of Structure and Reactivity*, HarperCollins College Publisher, New York, 4th edn, 1993.